

Measuring mechanical anisotropy of the cornea with Brillouin microscopy

Amira M. Eltony¹, Peng Shao^{1,+}, and Seok-Hyun Yun^{1,2,*}

¹Harvard Medical School and Wellman Center for Photomedicine, Massachusetts General Hospital, Boston, MA, 02114, USA

²Harvard-MIT Health Sciences and Technology, Cambridge, MA, 02139, USA

⁺Present affiliation: Intelon Optics Inc., Lexington, MA, 02421, USA

*syun@hms.harvard.edu

ABSTRACT

Load-bearing tissues are typically fortified by networks of protein fibers, often with preferential orientations. This fiber structure imparts the tissues with direction-dependent mechanical properties optimized to support specific external loads. To accurately model and predict tissues' mechanical response, it is essential to characterize the anisotropy on a microstructural scale. Previously, it has been difficult to measure the mechanical properties of intact tissues noninvasively. Here, we use Brillouin optical microscopy to visualize and quantify the anisotropic mechanical properties of corneal tissues at different length scales. We derive the stiffness tensor for a lamellar network of collagen fibrils and use angle-resolved Brillouin measurements to determine the longitudinal stiffness coefficients (longitudinal moduli) describing the *ex vivo* porcine cornea as a transverse isotropic material. Lastly, we observe significant mechanical anisotropy of the human cornea *in vivo*, highlighting the potential for clinical applications of off-axis Brillouin microscopy.

Introduction

Biological soft tissues are typically fiber-reinforced composites, consisting of a network of collagen and/or elastin fibers embedded in a hydrated matrix. In load-bearing regions, such as muscles, blood vessel walls, or the lining of the gastrointestinal tract, this microstructure imparts tissues with their unique combination of high flexibility and strength. Preferential fiber alignment is a natural consequence of the fiber structure conforming to resist the directional stresses and strains acting on a particular organ, resulting in anisotropic mechanical properties. Biaxial tensile testing has identified mechanical anisotropy in tissue samples excised from the lungs^{1,2}, the pulmonary arteries³, the pericardium⁴, the aorta⁵, the retina⁶, the vagina⁷, and the skin^{8,9} among others. The anisotropic behavior of these tissues is fine-tuned for their specific physiological functions. As such, fibrillar remodeling, resulting in changing tissue anisotropy, is often an indication of disease. There has been sustained interest in characterizing the mechanical anisotropy of soft tissues, particularly at the microstructural scale, in order to build accurate constitutive models which can be used to predict the tissues' response to mechanical loading¹⁰.

Brillouin microscopy is an emerging optical technique for biomechanical characterization of cells and tissues¹¹. The technique is based on inelastic light scattering from naturally-occurring (spontaneous) or stimulated acoustic waves in the material being probed. The resulting frequency shift of the scattered light, or the Brillouin frequency shift, is related to the acoustic wave speed and hence the elastic properties of the material. By employing a focused laser beam, Brillouin microscopy is able to map elastic properties with optical-scale spatial resolution ($\sim\mu\text{m}$). Brillouin microscopy has been used to measure localized mechanical changes in the eyes of patients with the corneal disease keratoconus¹², and depth-dependent mechanical

changes induced by collagen crosslinking (CXL)¹³. Brillouin scattering has revealed anisotropic properties of solid-state materials¹⁴, silks¹⁵, and plant stems¹⁶, but to our knowledge, has not yet been used to analyze soft biological tissue such as the cornea.

The cornea has anisotropic mechanical properties because of preferential fibril alignment tangential to the surface of the eye. The mechanical strength, shape, and transparency of the cornea stem from its microstructure: an intricate lattice of collagen fibrils embedded in a gel matrix. Characterizing corneal anisotropy is important in predicting the response of the cornea to different mechanical stimuli. Measuring the degree of anisotropy may also be a useful indicator of changes in the cornea's collagen organization due to disease or following surgical intervention^{17–19}. Some evidence of corneal anisotropy in the porcine eye has been obtained using ultrasound supersonic shear wave imaging²⁰, although with limited sensitivity and spatial resolution. Uniaxial tensile testing²¹ and optical coherence elastography²² have also been applied to the cornea, but were limited to comparing elasticity in tangential directions.

In this work, we directly visualize the alternating elastic properties of crisscrossing fiber layers (lamellae) in the porcine cornea using a high-resolution Brillouin microscope and confirm the interpretation of this pattern using transmission electron microscopy (TEM). We then measure the corresponding mechanical anisotropy of the bulk porcine cornea using Brillouin microscopy which we find to be consistent with the microstructural-scale imaging. We derive a composite model for the lamellar network of collagen fibrils in the cornea and use our angle-resolved Brillouin measurements to determine the stiffness coefficients (longitudinal moduli) describing the transverse isotropic tissue. Finally, we analyze the angle-dependent Brillouin corneal maps of healthy human subjects *in vivo* and determine the mechanical anisotropy of the normal human cornea.

Results

Composite model of corneal anisotropy

The stroma, which makes up the bulk of the cornea and contributes most to its biomechanical properties, is organized into layers approximately 2–3 μm thick called lamellae. Within each lamella, collagen fibrils of ~ 25 nm-diameter are co-aligned tangentially to the corneal surface²³. X-ray diffraction measurements suggest that collagen fibrils do not form a perfect crystalline lattice, but instead exhibit short-range order²⁴. However, for the purpose of modeling, the fibril organization within an individual lamella can be well approximated by a pseudo-hexagonal lattice²⁵. X-ray diffraction studies have established that the fibril diameter is 31 nm (humans) and 37 nm (pigs) and the interfibrillar Bragg spacing is 55 nm (humans) and 59 nm (pigs), corresponding to a fibril volume fraction $V^{(f)}$ of 0.22 (humans) and 0.28 (pigs)²⁵.

A single corneal lamella can be modelled as an aligned fiber composite, with the 1-direction oriented parallel to the fiber axis, and the 2- and 3-directions orthogonal to it (Fig. 1A). Since a collagen fibril can be assumed to be radially symmetric, it has transverse isotropic symmetry, and its stiffness tensor, $\mathbf{C}^{(f)}$, has five independent coefficients (see Supplementary Materials). Likewise, the gel matrix surrounding the fibrils can also be described with a stiffness tensor, $\mathbf{C}^{(m)}$. Assuming the fibers do not slip within the matrix under 1-directional loading (isostrain) and the stress is distributed equally across the fibers and matrix

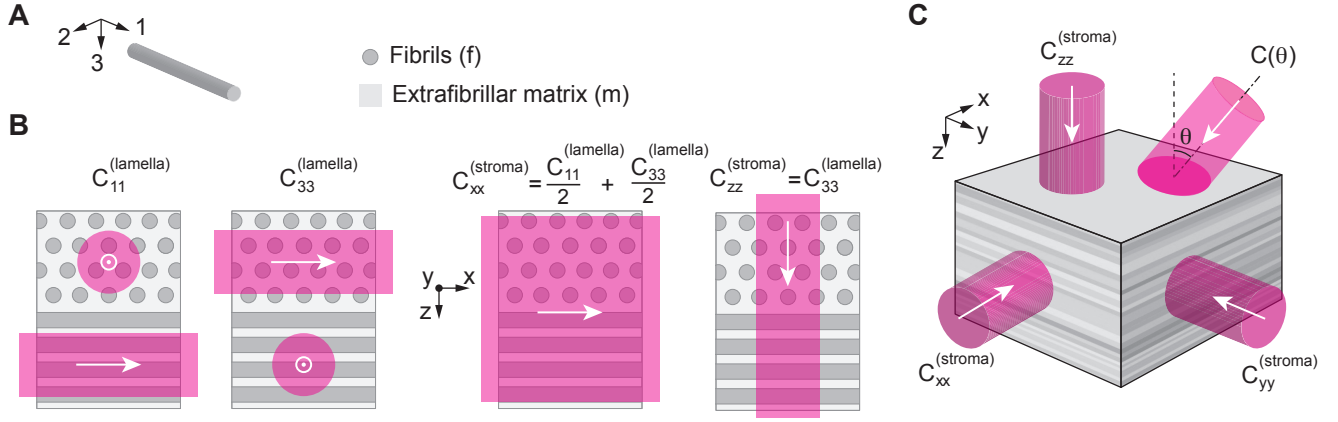


Figure 1. Brillouin measurements at different laser incidence angles detect tissue anisotropy. **A**, Within each lamella, collagen fibers (f) are co-aligned within a gel matrix (m). We define a coordinate system (1, 2, 3) for each lamella in which the 1-direction is always aligned with the fibril axis. **B**, The elastic modulus in the 1-direction C_{11} is different than the moduli orthogonal to the fibril axis, C_{22} and C_{33} . By reducing the laser spot size, it is possible to resolve individual lamellae using Brillouin microscopy. When the laser spot size covers multiple lamellae, we measure a combined modulus. For the bulk stroma we define the z -direction as orthogonal to the cornea and the $x - y$ plane as tangential. **C**, Cut-away view through the stromal depth showing stacked lamellae. The cornea is mechanically anisotropic, meaning that the longitudinal moduli (C_{ii}) have directional dependence. This can be probed using Brillouin microscopy with varying laser incidence angle θ .

during 2- and 3-directional loading (isostress), the stiffness coefficients along the 1, 2, and 3 directions, or longitudinal moduli, of a single lamella (Fig. 1B) can be expressed as a function of the individual moduli of the fibers (f) and of the extrafibrillar matrix (m) (law of mixtures): $C_{11}^{(\text{lamella})} = C_{11}^{(f)}V^{(f)} + C_{11}^{(m)}(1 - V^{(f)})$, $\frac{1}{C_{22}^{(\text{lamella})}} = \frac{V^{(f)}}{C_{22}^{(f)}} + \frac{1-V^{(f)}}{C_{22}^{(m)}}$, $\frac{1}{C_{33}^{(\text{lamella})}} = \frac{V^{(f)}}{C_{33}^{(f)}} + \frac{1-V^{(f)}}{C_{33}^{(m)}}$, where $C_{22}^{(m)} = C_{33}^{(m)}$ and $C_{22}^{(f)} = C_{33}^{(f)}$ by symmetry. An individual lamella is thus transverse isotropic with plane of symmetry 2-3 (i.e. orthogonal to the fibril axis).

The corneal stroma is composed of a stack of 300-500 lamellae of varying orientations. The axes of the collagen fibrils in successive lamellae are not truly random, but tend to lie along orthogonal meridians in the medial-lateral and superior-inferior directions, particularly in the posterior cornea²⁴. For simplicity, we model the stroma as a stack of layers with half oriented in the medial-lateral direction and half in the superior-inferior direction, which yields:

$$C_{xx}^{(\text{stroma})} = C_{yy}^{(\text{stroma})} = \frac{1}{2}C_{11}^{(\text{lamella})} + \frac{1}{2}C_{33}^{(\text{lamella})} \quad (1a)$$

$$C_{zz}^{(\text{stroma})} = C_{22}^{(\text{lamella})} = C_{33}^{(\text{lamella})} \quad (1b)$$

Here, the (x, y, z) coordinate system is defined in real space such that the z -direction is orthogonal to the cornea, and the x - and y -directions are tangential (medial-lateral and superior-inferior, Fig. 1B). In this model, the cornea is transverse isotropic with plane of symmetry x - y (i.e. tangential to the cornea).

For backward Brillouin light scattering spectroscopy with probe light entering the corneal tissue at an angle θ to the optic axis (Fig. 1C), the Brillouin frequency shift Ω is given by: $\Omega(\theta) = \frac{2n(\theta)v(\theta)}{\lambda} = \frac{2n(\theta)}{\lambda} \sqrt{\frac{C(\theta)}{\rho}}$, where $n(\theta)$ is the index of refraction of the material, λ is the wavelength of light, $v(\theta) = \sqrt{C(\theta)/\rho}$ is the longitudinal-wave acoustic speed, and $C(\theta)$ is

the effective longitudinal modulus of the stroma at angle θ to normal. For simplicity, we consider a case where the incident beam is in the x - z plane. The formalism described below can be applied to other tilt directions with appropriate coordinate transformations.

The index of refraction in the cornea is known to differ slightly depending on the direction of light propagation. Mueller matrix ellipsometry of the human cornea *in vivo* found that $n_x - n_z = 1.4 \times 10^{-4}$,²⁶ similar to other measurements²⁷). If individual lamellae are modelled as uniaxial birefringent layers stacked orthogonally, then $n_x - n_z = 2.8 \times 10^{-4}$ theoretically for a single lamella²⁸. As we will see, the contribution of this magnitude of birefringence to the Brillouin shift is 2-3 orders of magnitude lower than that of mechanical anisotropy. Therefore, we can neglect the birefringence and assume $n(\theta)$ to be a constant independent of θ .

An exact analytic expression for $C(\theta)$ can be written in terms of the stiffness tensor coefficients (Supplementary Materials). In the case of weak transverse isotropy, i.e. $C_{xx}^{(\text{stroma})} \approx C_{zz}^{(\text{stroma})}$, the effective longitudinal modulus can be expressed (Supplementary Materials) as: $C(\theta) \approx C_{zz} + (C_{xx} - C_{zz}) \sin^4 \theta + 2(C_{xz} + 2G_{yz} - C_{zz}) \sin^2 \theta \cos^2 \theta$, where the superscripts were ignored, and $G_{yz} (\ll C_{zz})$ is shear modulus of the stroma in the y - z plane. We confirm $C(0) = C_{zz}$, and $C(\pi/2) = C_{xx}$ (the beam is tilted toward the x -axis). The difference of these two values characterizes the magnitude of anisotropy of the tissue. We introduce anisotropic parameters, ϵ_{xx} and δ , defined as follows:

$$\epsilon_{xx} = C_{xx}/C_{zz} - 1 \quad (2a)$$

$$\delta = (C_{xz} + 2G_{yz})/C_{zz} - 1 \quad (2b)$$

Thus, we can write

$$C(\theta) = C_{zz} (1 + \epsilon_{xx} \sin^4 \theta + 2\delta \sin^2 \theta \cos^2 \theta) \quad (3)$$

The anisotropic coefficients are analogous, but not identical, to the Thomson parameters used to describe seismic anisotropy (Note: Thomson parameters are defined in terms of wave speeds rather than elastic moduli)²⁹.

Putting Eq. 1 into Eq. 2, we find:

$$\epsilon_{xx}^{(\text{stroma})} = \frac{(C_{11}^{(\text{lamella})} + C_{33}^{(\text{lamella})})/2}{C_{33}^{(\text{lamella})}} - 1 = \frac{1}{2} \epsilon_{11}^{(\text{lamella})} \quad (4)$$

Here $\epsilon_{11}^{(\text{lamella})}$ corresponds to the anisotropic parameter of a single lamella (with weak anisotropy $C_{33}^{(\text{lamella})} \approx C_{11}^{(\text{lamella})}$). It can be further shown that

$$\epsilon_{11}^{(\text{lamella})} = [\beta_2 V^{(f)} + \beta_1 (1 - V^{(f)})][\beta_1 V^{(f)} + 1 - V^{(f)}]/\beta_1 - 1, \quad (5)$$

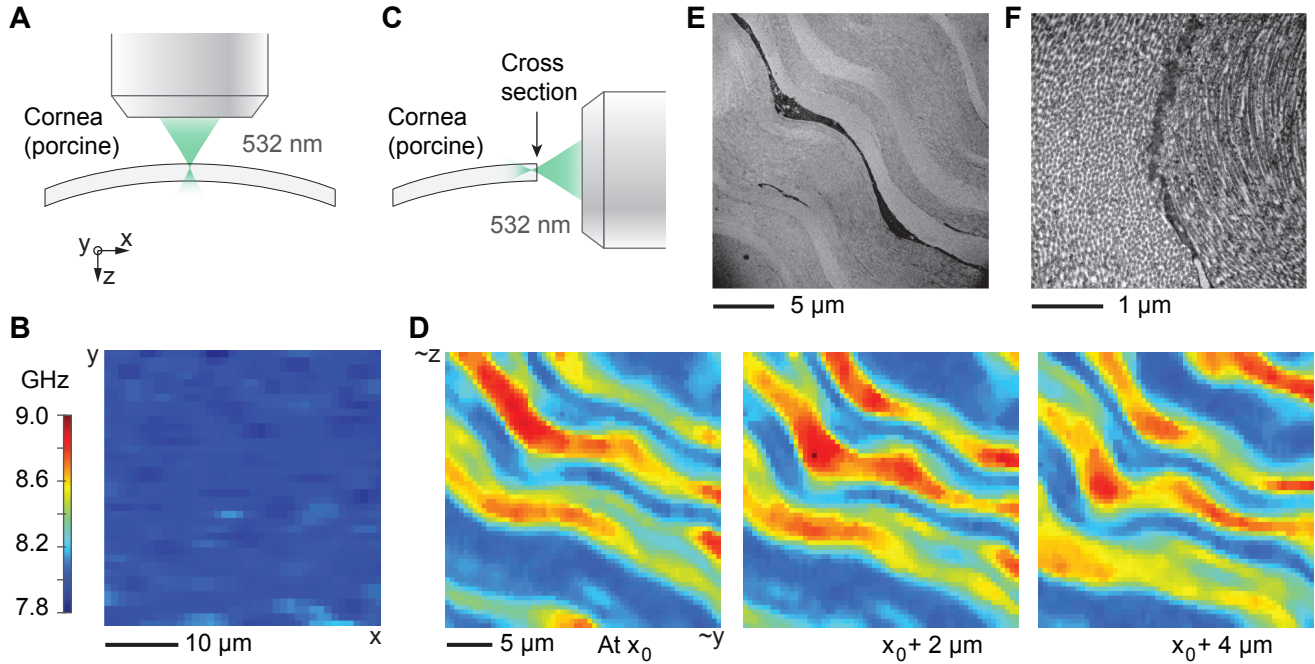


Figure 2. High-resolution Brillouin imaging of *ex vivo* porcine cornea. **A**, Schematic showing en face Brillouin imaging of the cornea using a 532 nm laser focused to a spot size of approximately 0.5 μm . **B**, Brillouin image of *ex vivo* porcine cornea measured en-face, showing relatively uniform Brillouin value across the x - y plane. **C**, Schematic showing Brillouin imaging of the corneal cross-section. The laser was focused just below the surface of the cross-section. **D**, Brillouin images of corneal cross-section at three different (relative) depths, revealing a lamellar pattern. **E** Transmission electron microscopy (TEM) image of corneal cross-section showing individual lamellae with alternating fibril orientations. A keratocyte is visible in between the two lamellae at the center of the image (keratocyte appears black with substructure). **F**, Higher resolution TEM image of the same region. Individual collagen fibrils can be seen aligned to the preferred directions in two adjacent lamellae.

where we have set $C_{11}^{(m)} = \beta_1 C_{33}^{(f)}$ and $C_{11}^{(f)} = \beta_2 C_{33}^{(f)}$.

Brillouin imaging of individual corneal lamellae

To test if Brillouin microscopy can indeed detect the anisotropy of individual lamellae, we excised corneas from porcine eyes within 4 hours of sacrifice. First, a corneal flap was measured en-face and imaged using an inverted confocal Brillouin microscope (Fig. 2A). In this orientation, the laser is orthogonal to almost all collagen fibrils, so we expect the lamellar contrast to disappear. Indeed, the resulting Brillouin image is mostly uniform with a Brillouin value of 7.981 ± 0.078 GHz (mean \pm standard deviation, measured at 532 nm). En-face images taken at different depths were similar. Second, we cut the corneal flap across the middle and mounted it vertically, allowing the cross-section to be imaged from beneath using an inverted confocal Brillouin microscope with a lateral resolution of $\sim 0.5 \mu\text{m}$ (Fig. 2C). Stromal tissue with a cross-sectional area of $50 \mu\text{m} \times 50 \mu\text{m}$ located in the center and the middle third depth-wise was imaged (Fig. 2D). Lamellae in the middle third of the corneal stroma are predominantly orthogonally stacked with little interleaving, resulting in alternating layers of higher and lower elastic modulus (from $C_{11}^{(\text{lamella})}$ to $C_{33}^{(\text{lamella})}$). This pattern is evident in the Brillouin images which show ribbons of width 1 - 6 μm with alternating Brillouin values ranging from 8.011 ± 0.014 GHz to 8.940 ± 0.043 GHz.

Figure 2E-F shows TEM images of corneal cross-sections taken in a similar region (central area of cornea, middle of

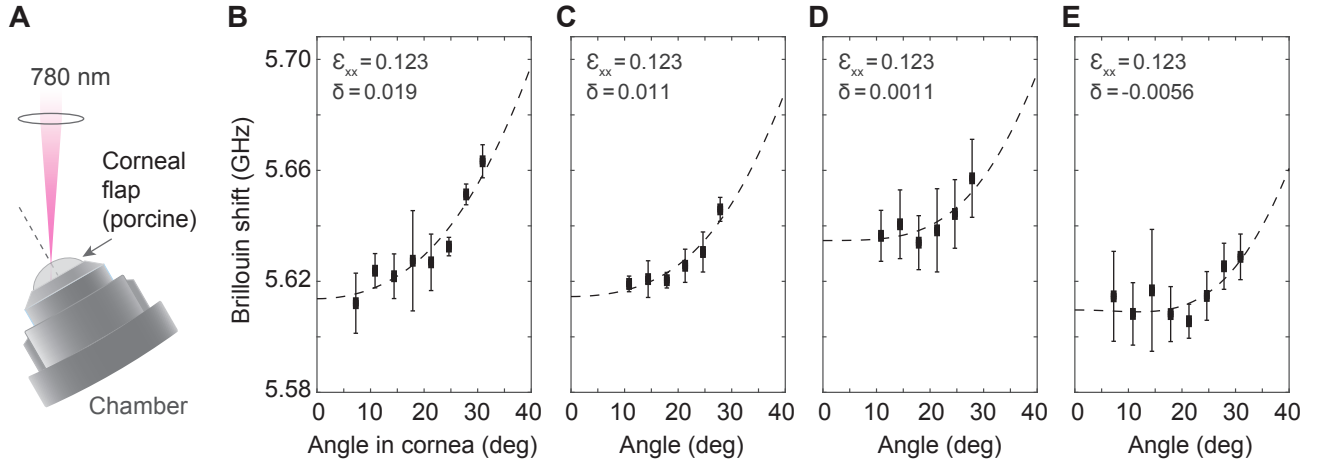


Figure 3. Measurement of Brillouin angle-dependence in *ex vivo* porcine cornea. **A**, Schematic showing Brillouin angle-dependence measurements of the cornea mounted in a Barron chamber using a 0.1-NA, 780 nm optical beam. **B-E**, Plots of Brillouin frequency shift (measured at 780 nm) for different in-tissue angles for 4 porcine samples (different animals), respectively. Boxes: measured mean. Error bars: standard deviation in three cycles of angle measurements. Dashed lines: best-fit curves using a fit parameter of δ , with the coefficient of determination $R^2 = 0.90$ (**B**), 0.92 (**C**), 0.78 (**D**), and 0.76 (**E**).

stromal depth) at two different magnifications. As expected, layers of alternating fibril orientation are visible. This lamellar structure is consistent with what we observed in the Brillouin images.

The inter-lamellar difference in the Brillouin frequency varied between corneas depending on the orientation of their cross-sections or, in other words, the orientation of collagen fibers with respect to the optical beam. The difference of 0.93 GHz was the maximum. The Brillouin value measured orthogonal to the lamella (Fig. 2B) is given by $C_{33}^{(\text{lamella})}$ and indeed found to be at its lowest (7.98 GHz). This maximum inter-lamellar contrast of 11.6% in Brillouin values (i.e. $\Omega(\pi/2)/\Omega(0) = 0.116$), corresponding to $\epsilon_{xx}^{(\text{lamella})} = C_{xx}/C_{zz} - 1 = (\Omega(\pi/2)/\Omega(0))^2 - 1 = 0.245$.

Angle-dependence of bulk cornea Brillouin measurements

The layered structure observed at the microscopic scale translates to a weak anisotropy of the bulk stroma, which we expected to see in larger-scale Brillouin measurements. For measurements of the intact cornea, we used a lower resolution (numerical aperture of ~ 0.1), near-infrared ($\lambda = 780$ nm) Brillouin imaging system³⁰. As before, corneal flaps were excised from porcine eye globes received within 4 hours of sacrifice. Intact corneal flaps were mounted in a Barron chamber which could be rotated about the corneal apex, allowing for different laser incidence angles onto the same location in the central cornea (Fig. 3A). Brillouin measurements of the central cornea were made at 6-8 different laser incidence angles for four different cornea samples (from four different pigs).

Results are shown in Fig. 3B-E. Angles in air were converted to angles in tissue assuming a stromal index of refraction of 1.376.³¹ The range of possible angles is limited by signal-to-noise ratio: at low angles, the elastic scattering background from Fresnel-type surface reflection becomes dominant over the Brillouin signal, while at large angles, the Brillouin signal is reduced due to beam aberration on refraction. From the cross-sectional imaging experiment described in the previous section, we have

measured $\epsilon_{xx}^{(\text{lamella})}$ to be 0.245. Using Eq. 4, we determined $\epsilon_{xx}^{(\text{stroma})}$ to be 0.123. We used this value in the weak transverse isotropy model (Eq. 3) to fit the angle-dependence data, with free parameters $\nu(0) = \sqrt{C_{zz}/\rho}$ and δ . Agreement with the model was fairly good, with R^2 ranging from 0.76 to 0.92 for the different samples.

Anisotropy *in vivo* in Brillouin maps of the human cornea

We also found evidence of corneal anisotropy in Brillouin measurements of human subjects. Study participants with normal corneas were scanned using a custom-built Brillouin imaging system at a wavelength of 780 nm³⁰. When a human subject is imaged using this instrument, the subject's gaze angle is directed towards a stationary fixation target while the Brillouin interface is translated right-left and up-down to measure different locations laterally across the cornea. Because the optical path

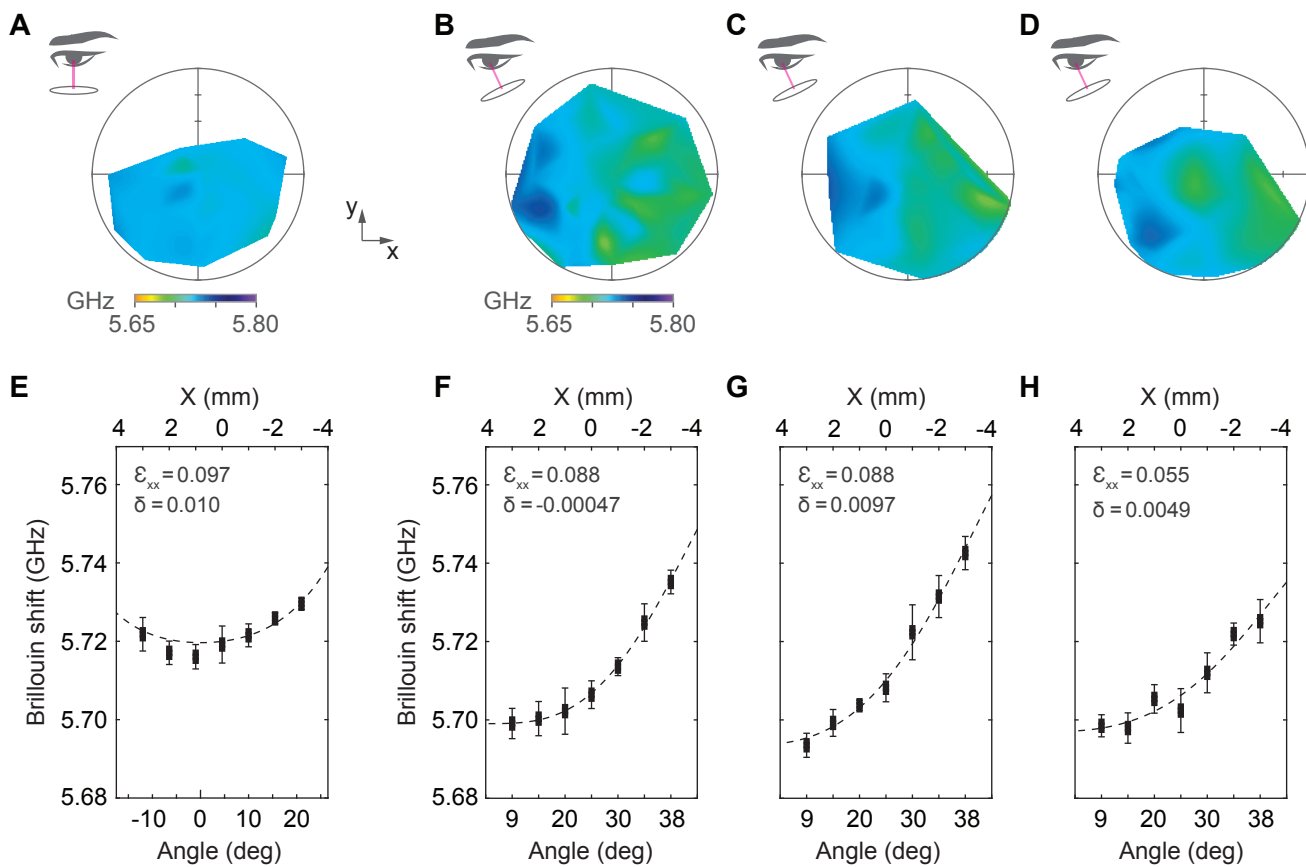


Figure 4. Anisotropy *in vivo* in Brillouin maps of the human cornea. **A**, Brillouin frequency shift map of a normal subject with laser incidence angle close to 0° at the corneal apex (see diagram at left). **B-D**, Brillouin maps of three normal subjects for a steeper set of laser incidence angles (see diagrams). **E**, Plot of Brillouin values for subject A integrated vertically over a zone $y = [-1 \text{ mm}, 1 \text{ mm}]$ versus x-coordinate (upper axis) and computed incidence angle (lower axis). The plot shows slightly increasing Brillouin shift with increasing $|x|$, due to corneal anisotropy: the laser-cornea incidence angle varies slightly as the laser is translated in x (left-right) to create the Brillouin map due to corneal curvature. **F-H**, Vertically-integrated plots for subjects B-D (respectively). In this configuration, the laser-cornea incidence angle increases continuously as the laser is translated from right to left to create the Brillouin map. The apparent Brillouin shift gradient from right to left is consistent with expected corneal anisotropy. Data (boxes: mean, error bars: standard deviation from the vertical averaging) were fit to the weak transverse isotropy model (Eq. 3) with ϵ_{xx} as an additional free parameter (dashed lines). Fitted values of ϵ_{xx} and δ are shown, where $R^2 = 0.96$ (A), 0.998 (B), 0.99 (C), 0.94 (D).

is rigidly fixed with respect to the interface, as the laser position changes, the angle of incidence (relative to the corneal surface) also changes. When the laser incidence angle is close to 0° , this change is small, but for larger tilt angles there is a gradually increasing angle of incidence as the laser moves from right to left across the cornea (Fig. 4).

Data from approximately 30 axial scans were combined to create a color-coded map of the mean Brillouin shift laterally across the corneal stroma. An increasing Brillouin gradient from right to left is apparent in the resulting maps, with larger Brillouin values for larger incidence angles as we would expect. The Brillouin maps of three different human subjects displaying this gradient are shown in Fig. 4B-D. By contrast, when the laser angle is changed to minimize the variation in incidence angle (Fig. 4A), the resulting Brillouin map is more uniform with no obvious gradient.

To analyze the angle-dependence inherent in the human maps, Brillouin values were integrated vertically over a range within ± 1 mm from the horizontal center line ($y = 0$), and the x -coordinates were converted to approximate angles assuming a spherical corneal surface with 7.7 mm radius-of-curvature. This allowed us to fit the same weak transverse isotropy model that was used for the porcine samples. The fitted anisotropic parameter $\epsilon_{xx}^{(\text{stroma})}$ values for these human corneas range from 0.055 to 0.097.

Longitudinal stiffness coefficients of the cornea

From the angle-resolved Brillouin measurements of the porcine and human corneas we can estimate the longitudinal moduli. Data were fit to the weak transverse isotropy model (Eq. 3), yielding fitted values for $\Omega(0) = \frac{2n}{\lambda} \sqrt{C_{zz}/\rho}$, $\epsilon_{xx} = C_{xx}/C_{zz} - 1$, and $\delta = (C_{xz} + 2G_{yz})/C_{zz} - 1$. Assuming a stromal index of refraction³¹ of 1.376 and a mass density³² of 1.05 g cm^{-2} , we extracted all three longitudinal moduli C_{zz} and $C_{xx} = C_{yy}$ for each sample as well as the combination of moduli $C_{xz} + 2G_{yz}$ ($\approx C_{xz}$) (Table 1). The symmetry of transverse isotropy dictates that $C_{yz} = C_{xz}$ and $C_{xy} = C_{xx} - 2G_{xy} \approx C_{xx}$. Therefore, all the longitudinal stiffness coefficients C_{ij} 's ($i, j = x, y, z$) have been determined.

It is interesting to compare the two species. The human corneas exhibited greater out-of-plane stiffness C_{zz} than the porcine corneas. The in-plane stiffness, C_{xx} and C_{yy} , however, were nearly the same between human and porcine corneas. As a result, the human corneas have a lower degree of anisotropy than the porcine corneas.

The anisotropic parameters we determined from measurements of porcine and human corneas can be used in our composite model to estimate the properties of the cornea's constituent parts: collagen fibrils and gel matrix. The gel matrix in particular has not previously been accessible for material characterization. The mean anisotropic parameter measured in humans was $\epsilon_{xx}^{(\text{stroma})} = 0.082 \pm 0.018$ (4 subjects), corresponding to $\epsilon_{xx}^{(\text{lamella})}(\text{human}) = 0.164$ (Supplementary Materials). For porcine samples, we measured $\epsilon_{xx}^{(\text{lamella})}(\text{human}) = 0.245$. Considering the different fibril volume fractions²⁵, $V^{(f)}(\text{human}) = 0.22$ and $V^{(f)}(\text{porcine}) = 0.28$, and assuming that the material properties of the collagen fibrils and gel matrix are similar between humans and pigs (specifically, β_1, β_2 values within 5%), we can estimate the ratio of the longitudinal modulus in the axial '1' direction (along the fiber) to that in the transverse '2,3' directions (orthogonal to the fiber), $\beta_2(\text{human}) = C_{11}^{(f)}/C_{33}^{(f)} = 1.37$ and $\beta_2(\text{porcine}) = 1.44$ (Eq. 5). Similar values have been reported in ultrasound measurements of collagen from the bovine Achilles tendon which found $C_{11}^{(f)}/C_{33}^{(f)} = 1.47$ (fixed)³³, $C_{11}^{(f)}/C_{33}^{(f)} = 1.33$ (fresh)³⁴. Likewise, we estimate that the ratio of the

longitudinal modulus of the gel matrix (assumed isotropic) to that of the fiber (in the transverse direction) is $\beta_1(\text{human}) = C_{11}^{(m)}/C_{33}^{(f)} = 0.61$ and $\beta_1(\text{porcine}) = 0.58$, suggesting that the mechanical contrast between matrix and fibers is relatively low in the transverse direction.

Stiffness coefficients	Porcine <i>ex vivo</i> (GPa)	Human <i>in vivo</i> (GPa)
C_{zz}	2.662 ± 0.011	2.743 ± 0.011
C_{xx}, C_{yy}	2.971 ± 0.012	2.968 ± 0.059
$C_{xz} + 2G_{yz}$	2.680 ± 0.029	2.759 ± 0.021

Table 1. Longitudinal elastic moduli for porcine corneas *ex vivo* (at ~ 23 °C) and human corneas *in vivo* measured by angle-resolved Brillouin measurements ($\lambda = 780$ nm). Mean \pm standard deviation from 4 samples in each group.

Discussion

We have demonstrated that individual stromal lamellae can be resolved based on their Brillouin shift contrast. This contrast arises directly from the anisotropic elastic properties of the lamellae stemming from their fibrillar organization. We derived a composite model describing the lamellar network of collagen fibrils in the cornea. In aggregate, the crisscrossing lamellae produce a weakly transverse isotropic stroma. We confirmed that the Brillouin frequency shift of the cornea is indeed angle-dependent. Results agree fairly well with our composite model using the anisotropic parameter ($\epsilon_{xx}^{(\text{stroma})}$) derived from lamellar-scale Brillouin data. While techniques such as TEM have previously elucidated the fibrillar architecture of the cornea, this work uniquely characterizes the elastic properties of the cornea at the microstructural scale, allowing us to estimate the stiffness coefficients (longitudinal moduli) describing the transverse isotropic tissue. This material information is useful for detailed numerical simulations of the cornea. Equally important, we were able to connect the properties at the micro-scale to those of the bulk cornea, a critical link for understanding the impact of diseases or surgeries that alter the collagen structure.

Fiber-reinforced composite materials are ubiquitous in the body, where their mechanical properties serve their physiological functions. For example, the tympanic membrane of the ear has a lamellar collagen structure similar to that of the cornea and is also mechanically anisotropic³⁵. A challenge in reconstructive ear surgery is replicating the complex, anisotropic material properties of the tympanic membrane so that the frequency response and mode shapes required for hearing can be restored³⁶. Recent studies have explored laser-induced collagen remodeling as a treatment for chronic inflammatory ear pathologies that aims to restore the intricate collagen network rather than replace it with a poorly-matched synthetic material³⁷. The microstructure of the uterine cervix also contains an anisotropic network of collagen fibers³⁸. Preterm birth is thought to be caused by premature weakening of the cervix under the increasing load of a growing fetus. Efforts are underway to better understand the collagen remodelling process that allows the cervix to become more pliable during gestation in order to devise prophylactics against preterm birth³⁹. Likewise, arterial walls have a network of layered collagen and elastin fibers with a predominantly circumferential orientation⁴⁰. Gradual collagen remodelling plays a major role in the weakening and rupture of abdominal aortic aneurysms, resulting in many deaths⁴¹. Current investigations into the structure-function relationships in

soft tissues like these primarily rely on traditional mechanical techniques such as indentation or video extensometry. These techniques cannot probe the micro-scale elastic properties of the tissue, cannot typically probe all axes, and are often difficult to implement *in vivo*. Multi-angle (vector) Brillouin microscopy may find application in characterizing the anisotropic mechanical properties of fiber-composite tissues found throughout the body with high spatial resolution.

Another potential avenue of application is biomaterial design. Tissue engineered constructs must be able to closely mimic the *in-vivo* mechanical and structural properties of the tissues they aim to replace. Because many soft tissues exhibit intricate fiber networks with preferential fiber alignment, they typically have complex, anisotropic mechanical properties. This has been recognized and biomaterials that can imitate soft-tissue mechanical anisotropy have been a goal of tissue engineering for more than a decade⁴²⁻⁴⁴). Brillouin microscopy could provide valuable material data for designing engineered biomaterials and then characterizing the resulting constructs.

Lastly, we observed significant directional dependence in human Brillouin maps measured *in vivo*. The ~35 MHz gradient over the angle of 0 to 40 deg is comparable to the magnitude of spatial variation detected in mild corneal disease³⁰. Therefore, the angle dependence must be taken into account in the interpretation of raw measurement data. In principle, it can be removed by numerical correction or beam scanning with a constant incident angle. On the other hand, because the anisotropy is a direct result of the fibrillar structure of the cornea, analyzing the angle-dependence or mechanical anisotropy may be a useful metric to detect disruption or remodelling of the regular collagen lattice due to disease or surgical intervention. We expect the Brillouin angle-dependence to decrease in degenerative conditions where the lamellar or fibrillar microstructure becomes disorganized. It would be interesting to measure the Brillouin angle-dependence in the cone region of a keratoconus cornea.

Methods

Cross-sectional Brillouin measurements

Porcine eye globes were received on ice within 4 hours of sacrifice and corneal flaps were immediately excised. A custom 3D-printed fixture was used to mount the corneal flap securely so that a clean slice could be made through the center of the cornea using a scalpel. The resulting slice was then sandwiched between two glass slides so that the cross-section abutted one edge of the slides. The slides and cornea were then mounted vertically in a custom-made holder atop a glass-bottom dish so that the corneal cross-section was optically accessible from below. Empty space in the glass bottom dish and between the slides was filled with corneal preservation medium to prevent drying of the corneal slice. The corneal cross-section was imaged using a confocal Brillouin microscope with a 532 nm laser and a two-stage, apodized, virtually imaged phased array (VIPA) spectrometer; this instrument has been described previously⁴⁵. A co-aligned bright-field microscope was used to navigate to the middle region of the corneal depth for measurement. The Brillouin measurement volume per point was approximately $0.5\ \mu\text{m} \times 0.5\ \mu\text{m} \times 1.0\ \mu\text{m}$ and the integration time used was 150 ms. For TEM analysis, corneal slices were fixed using K2 buffer and later imaged using a transmission electron microscope (model CM10, Philips Electron Optics, Eindhoven, The Netherlands).

Brillouin angle-dependence measurements

Corneal flaps with a 2-3 mm scleral ring were excised from porcine eye globes using a pair of curved scissors and placed in Carry-C corneal preservation medium (Alchimia S.r.l., Padua, Italy) at room temperature (22 - 24 °C). To minimize perturbation of the cornea, the iris was not forcibly removed but was instead left attached to the corneal flap. For imaging, the intact corneal flap was mounted in a Barron chamber (Katena Products Inc., New Jersey, USA) filled with Carry-C corneal preservation medium (Alchimia S.r.l., Padua, Italy), which set an effective intraocular pressure (IOP) of about 15 mmHg, confirmed using a standard water column. For these measurements we used a different Brillouin instrument designed for whole-cornea imaging *in vivo* at a wavelength of 780 nm. This instrument has been described previously³⁰. The Barron chamber was mounted on a rotation stage (RP01, Thorlabs Inc., New Jersey, USA) so that the laser incidence angle could be adjusted. A small ink mark was used as a target to insure that the measurement point remained fixed on the corneal apex as the angle varied. The Brillouin measurement volume per point was approximately $2\mu\text{m} \times 2\mu\text{m} \times 30\mu\text{m}$ and the integration time used ranged from 200-700 ms. The Brillouin value at each angle is obtained by averaging points measured throughout the stromal depth. To minimize the impact of environmental drifts, the cycle of angle measurements was repeated three times and the resulting Brillouin values at each angle were averaged.

Brillouin maps of human subjects

Healthy subjects with normal corneas were imaged at two locations: the Institute for Refractive and Ophthalmic Surgery (IROC) in Zürich, Switzerland, and the Woolfson Eye Institute in Atlanta, Georgia, following approval from the Institutional Review Board (IRB) of Partners HealthCare, the Partners Human Research Committee (PHRC), the Institutional Review Board of IROC, Zürich, and the Woolfson Eye Institute Ethics Committee. Informed consent was obtained from every patient before imaging and all experiments were performed in accordance with the principles of the Declaration of Helsinki. In this study, a 'normal cornea' was classified as: less than 3 diopters refractive error, corneal thickness between 495 and 600 μm , normal corneal topography, no corneal pathology, and no history of eye disease. Study participants were scanned using a clinical Brillouin imaging system at a wavelength of 780 nm which has been described previously³⁰. The system specifications are the same as the instrument used for porcine angle-dependence measurements but in a mobile unit. For human subjects, axial scans were taken at ~ 30 different locations across the cornea with an integration time of 300 ms per point, or 12 s per scan. Brillouin shift values were averaged through the stromal depth, yielding a single Brillouin value per location. A color-coded Brillouin map was then created by 2-dimensional interpolation between these points.

Statistical Analysis

Data fitting was performed using the Curve Fitting Toolbox in MATLAB (MathWorks Inc., Massachusetts, USA) with the nonlinear least squares method. The R-squared (coefficient of determination) was used as a measure of the global fit of the model.

Data Availability

The data that support the findings of this study are available from the corresponding author upon reasonable request.

References

1. Vawter, D. L., Fung, Y. C. & West, J. B. Elasticity of excised dog lung parenchyma. *J. Appl. Physiol.* **45**, 261–269 (1978).
2. Vawter, D. L., Fung, Y. C. & West, J. B. Constitutive Equation of Lung Tissue Elasticity. *J. Biomech. Eng.* **101**, 38–45 (1979).
3. Debes, J. C. & Fung, Y. C. Biaxial mechanics of excised canine pulmonary arteries. *Am. J. Physiol. - Hear. Circ. Physiol.* **269**, H433–H442 (1995).
4. Lee, M. C., LeWinter, M. M. & Freeman, G. Biaxial mechanical properties of the pericardium in normal and volume overload dogs. *Am. J. Physiol. - Hear. Circ. Physiol.* **18**, H222–H230 (1985).
5. Zhou, J. & Fung, Y. C. The degree of nonlinearity and anisotropy of blood vessel elasticity. *Proc. Natl. Acad. Sci.* **94**, 14255–14260 (1997).
6. Chen, K., Rowley, A. P. & Weiland, J. D. Elastic properties of porcine ocular posterior soft tissues. *J. Biomed. Mater. Res. - Part A* **93**, 635–645 (2009).
7. Martins, P. *et al.* Prediction of nonlinear elastic behaviour of vaginal tissue: experimental results and model formulation. *Comput. Methods Biomech. Biomed. Eng.* **13**, 327–337 (2010).
8. Lanir, Y. & Fung, Y. C. Two-dimensional mechanical properties of rabbit skin-I. Experimental system. *J. Biomech.* **7**, 29–34 (1974).
9. Ní Annaidh, A., Bruyère, K., Destrade, M., Gilchrist, M. D. & Otténio, M. Characterising the Anisotropic Mechanical Properties of Excised Human Skin Aisling. *J. Mech. Behav. Biomed. Mater.* **5**, 139–148 (2012).
10. Holzapfel, G. A. Biomechanics of Soft Tissue. In Lemaitre, J. (ed.) *Handbook of Materials Behavior Models*, Volume III, Section 10.11, 1057–1071 (Academic Press, San Diego, CA, 2001).
11. Scarcelli, G. & Yun, S. H. Confocal Brillouin microscopy for three-dimensional mechanical imaging. *Nat. Photonics* **2**, 39–43 (2008).
12. Scarcelli, G., Besner, S., Pineda, R., Kalout, P. & Yun, S. In Vivo Biomechanical Mapping of Normal and Keratoconus Corneas. *JAMA Ophthalmol.* **133**, 480–482 (2015).
13. Scarcelli, G. *et al.* Brillouin Microscopy of Collagen Crosslinking: Noncontact Depth-Dependent Analysis of Corneal Elastic Modulus. *Investig. Ophthalmol. Vis. Sci.* **54**, 1418–1425 (2013).
14. Koski, K. J., Akhenblit, P., McKiernan, K. & Yarger, J. L. Non-invasive determination of the complete elastic moduli of spider silks. *Nat. Mater.* **12**, 262–267 (2013).

15. Zhang, Y. *et al.* The elastic constants of rubrene determined by Brillouin scattering and density functional theory. *Appl. Phys. Lett.* **110** (2017).
16. Elsayad, K. *et al.* Mapping the subcellular mechanical properties of live cells in tissues with fluorescence emission-Brillouin imaging. *Sci. Signal.* **9**, 1–13 (2016).
17. Meek, K. M. *et al.* Changes in Collagen Orientation and Distribution in Keratoconus Corneas. *Investig. Ophthalmol. Vis. Sci.* **46**, 1948–1956 (2005).
18. Morishige, N. *et al.* Second-Harmonic Imaging Microscopy of Normal Human and Keratoconus Cornea. *Investig. Ophthalmol. Vis. Sci.* **48**, 1087–1094 (2007).
19. Meek, K. M. & Boote, C. The use of X-ray scattering techniques to quantify the orientation and distribution of collagen in the corneal stroma. *Prog. Retin. Eye Res.* **28**, 369–392 (2009).
20. Nguyen, T. M., Aubry, J. F., Fink, M., Bercoff, J. & Tanter, M. In Vivo Evidence of Porcine Cornea Anisotropy Using Supersonic Shear Wave Imaging. *Investig. Ophthalmol. Vis. Sci.* **55**, 7545–7552 (2014).
21. Elsheikh, A. *et al.* Experimental Assessment of Corneal Anisotropy. *J. Refract. Surg.* **24**, 178–187 (2008).
22. Singh, M. *et al.* Investigating Elastic Anisotropy of the Porcine Cornea as a Function of Intraocular Pressure With Optical Coherence Elastography. *J. Refract. Surg.* **32**, 562–567 (2016).
23. Komai, Y. & Ushiki, T. The three-dimensional organisation of collagen fibrils in the human cornea and sclera. *Investig. Ophthalmol. Vis. Sci.* **32**, 2244–2258 (1991).
24. Meek, K. M. & Quantock, A. J. The Use of X-ray Scattering Techniques to Determine Corneal Ultrastructure. *Prog. Retin. Eye Res.* **20**, 95–137 (2001).
25. Meek, K. M. & Leonard, D. W. Ultrastructure of the corneal stroma: a comparative study. *Biophys. J.* **64**, 273–280 (1993).
26. Van Blokland, G. J. & Verhelst, S. C. Corneal polarization in the living human eye explained with a biaxial model. *J. Opt. Soc. Am. A* **4**, 82 (1987).
27. Shute, C. C. Haidinger's brushes and predominant orientation of collagen in corneal stroma. *Nature* **250**, 163–164 (1974).
28. Donohue, D. J., Stoyanov, B. J., McCally, R. L. & Farrell, R. A. Numerical modeling of the cornea's lamellar structure and birefringence properties. *J. Opt. Soc. Am. A* **12**, 1425 (1995).
29. Thomsen, L. Weak elastic anisotropy. *Geophysics* **51**, 1954–1966 (1986).
30. Shao, P. *et al.* Spatially-resolved Brillouin spectroscopy reveals biomechanical abnormalities in mild to advanced keratoconus in vivo. *Sci. Reports* **9**, 7467 (2019).
31. Fatt, I. & Weissman, B. A. Cornea I: Form, Swelling Pressure, Transport Processes, and Optics. In *Physiology of the Eye*, chap. 6, 97–149 (Elsevier Inc., Amsterdam, Netherlands, 1992), 2nd edn.

32. Leonard, D. W. & Meek, K. M. Refractive Indices of the Collagen Fibrils and Extrafibrillar Material of the Corneal Stroma. *Biophys. J.* **72**, 1382–1387 (1997).
33. Hoffmeister, B. K., Verdonk, E. D., Wickline, S. A. & Miller, J. G. Effect of collagen on the anisotropy of quasi-longitudinal mode ultrasonic velocity in fibrous soft tissues: A comparison of fixed tendon and fixed myocardium. *J. Acoust. Soc. Am.* **96**, 1957–1964 (1994).
34. Kuo, P. L., Li, P. C. & Li, M. L. Elastic properties of tendon measured by two different approaches. *Ultrasound Medicine Biol.* **27**, 1275–1284 (2001).
35. Lim, D. J. Human tympanic membrane: An ultrastructural observation. *Acta Oto-Laryngologica* **70**, 176–186 (1970).
36. Williams, K. R., Blayney, A. W. & Lesser, T. H. Mode shapes of a damaged and repaired tympanic membrane as analysed by the finite element method. *Clin. Otolaryngol. Allied Sci.* **22**, 126–131 (1997).
37. Schacht, S. A. L., Stahn, P., Hinsberger, M. & Schick, B. Laser-induced tissue remodeling within the tympanic membrane. *J. Biomed. Opt.* **23**, 1 (2018).
38. Yao, W. *et al.* Collagen fiber orientation and dispersion in the upper cervix of non-pregnant and pregnant women. *PLoS ONE* **11**, 1–20 (2016).
39. Shi, L. *et al.* Anisotropic Material Characterization of Human Cervix Tissue Based on Indentation and Inverse Finite Element Analysis. *J. Biomech. Eng.* **141**, 1–13 (2019).
40. O’Connell, M. K. *et al.* The Three-Dimensional Micro- and Nanostructure of the Aortic Medial Lamellar Unit Measured Using 3D Confocal & Electron Microscopy Imaging. *Matrix Biol.* **27**, 171–181 (2008).
41. Gasser, T. C. *et al.* Spatial orientation of collagen fibers in the abdominal aortic aneurysm’s wall and its relation to wall mechanics. *Acta Biomater.* **8**, 3091–3103 (2012).
42. Courtney, T., Sacks, M. S., Stankus, J., Guan, J. & Wagner, W. R. Design and analysis of tissue engineering scaffolds that mimic soft tissue mechanical anisotropy. *Biomaterials* **27**, 3631–3638 (2006).
43. de Mulder, E. L., Buma, P. & Hannink, G. Anisotropic Porous Biodegradable Scaffolds for Musculoskeletal Tissue Engineering. *Materials* **2**, 1674–1696 (2009).
44. Schwan, J. *et al.* Anisotropic engineered heart tissue made from laser-cut decellularized myocardium. *Sci. Reports* **6**, 1–12 (2016).
45. Scarcelli, G. *et al.* Noncontact three-dimensional mapping of intracellular hydromechanical properties by Brillouin microscopy. *Nat. Methods* **12**, 1132–1134 (2015).

Acknowledgements

The authors thank Dr. Theo Seiler and Dr. Doyle Stulting for obtaining the human data and Neema Kumar and Jie Zhao for assistance with sample preparation and TEM imaging. This study was supported by funding from the National Institutes of Health, grants R01-EY025454, P41-EB015903, R01-EB027653, and R41-EY028820.

Author contributions statement

A.M.E., P.S., and S.H.Y. designed the experiments. A.M.E. conducted the experiments and analyzed the data. A.M.E. and S.H.Y. wrote the manuscript.

Additional information

Competing interests A.M.E., P.S. and S.H.Y. hold issued and pending patents related to the technology. S.H.Y. is the scientific founder of Intelon Optics, Inc., which licensed the patents, and P.S. is currently an employee of the company.

Supplementary Materials for *Measuring mechanical anisotropy of the cornea with Brillouin microscopy*

Composite model of a corneal lamella

Let $\sigma_i^{(k)}$ and $s_j^{(k)}$ denote the i -th stress and j -th strain elements, respectively, in Voigt notation. Here, '1' is for 'xx', '2' for 'yy', '3' for 'zz', '4' for 'yz', '5' for 'xz', and '6' for 'xy' for Cartesian coordinates used to describe the cornea (Fig. 1C). On the other hand, '1' is for '11', '2' for '22', '3' for '33', '4' for '23', '5' for '13', and '6' for '12' for the 123-coordinate system defined with respect to a single collagen fibril (Fig. 1A). $C_{ij}^{(k)}$ denotes the ij -th elastic modulus for material ' k ', such that we have stress-strain relations of the form (Voigt notation):

$$\begin{bmatrix} \sigma_1^{(k)} \\ \sigma_2^{(k)} \\ \sigma_3^{(k)} \\ \sigma_4^{(k)} \\ \sigma_5^{(k)} \\ \sigma_6^{(k)} \end{bmatrix} = \begin{bmatrix} C_{11}^{(k)} & C_{12}^{(k)} & C_{13}^{(k)} & 0 & 0 & 0 \\ C_{12}^{(k)} & C_{22}^{(k)} & C_{23}^{(k)} & 0 & 0 & 0 \\ C_{13}^{(k)} & C_{23}^{(k)} & C_{33}^{(k)} & 0 & 0 & 0 \\ 0 & 0 & 0 & C_{44}^{(k)} & 0 & 0 \\ 0 & 0 & 0 & 0 & C_{55}^{(k)} & 0 \\ 0 & 0 & 0 & 0 & 0 & C_{66}^{(k)} \end{bmatrix} \begin{bmatrix} s_1^{(k)} \\ s_2^{(k)} \\ s_3^{(k)} \\ s_4^{(k)} \\ s_5^{(k)} \\ s_6^{(k)} \end{bmatrix} \quad (6)$$

We define a coordinate system for the lamella in which the 1-direction is parallel to the fibril axis, and the 2- and 3-directions are orthogonal to it (Fig. 1). For Brillouin measurements at a 180° angle, light scatters from longitudinal elastic waves which have displacement only along the direction of wave propagation. For example, an elastic wave propagating in the 1-direction has $s_2^{(k)} = s_3^{(k)} = 0$ and hence $\sigma_1^{(k)} = C_{11}^{(k)} s_1^{(k)}$.

First, consider the case of loading parallel to the fibril axis (1-direction). The stress in the composite is the sum of the stresses in all of the fibrils ($\sigma_1^{(f)}$) and in the extrafibrillar matrix ($\sigma_1^{(m)}$), weighted by their volume fractions (law of mixtures):

$$\sigma_1^{(\text{lamella})} = \sigma_1^{(f)} V^{(f)} + \sigma_1^{(m)} (1 - V^{(f)}) \quad (7)$$

If we assume that there is no slippage between the fibrils and the matrix, the strain of the fibers and the matrix must be equal (the 'isostrain rule'):

$$s_1^{(\text{lamella})} = s_1^{(f)} = s_1^{(m)} \quad (8)$$

Hence, the longitudinal modulus $C_{11}^{(\text{lamella})}$ is given by:

$$C_{11}^{(\text{lamella})} = C_{11}^{(f)} V^{(f)} + C_{11}^{(m)} (1 - V^{(f)}) \quad (9)$$

Likewise, in the case of loading perpendicular to the fiber axis, the fibrils and the matrix experience different strains, but equal stress ('isostress rule'):

$$\frac{1}{C_{22}^{(\text{lamella})}} = \frac{V^{(f)}}{C_{22}^{(f)}} + \frac{(1 - V^{(f)})}{C_{22}^{(m)}} \quad (10a)$$

$$\frac{1}{C_{33}^{(\text{lamella})}} = \frac{V^{(f)}}{C_{33}^{(f)}} + \frac{(1 - V^{(f)})}{C_{33}^{(m)}} \quad (10b)$$

If we assume that the extrafibrillar matrix is isotropic, $C_{11}^{(m)} = C_{33}^{(m)}$, and that the fibers are radially symmetric, $C_{22}^{(f)} = C_{33}^{(f)}$, we obtain:

$$C_{11}^{(\text{lamella})} = C_{11}^{(f)} V^{(f)} + C_{11}^{(m)} (1 - V^{(f)}) \quad (11a)$$

$$C_{22}^{(\text{lamella})} = C_{33}^{(\text{lamella})} = \frac{C_{11}^{(m)} V^{(f)} + C_{33}^{(f)} (1 - V^{(f)})}{C_{11}^{(m)} C_{33}^{(f)}} \quad (11b)$$

So we see that an individual lamella is transverse isotropic with plane of symmetry 2 – 3 (i.e. orthogonal to the fibril axis).

Model of an orthogonal stack of lamellae

To compute the properties of the bulk stroma, we sum over the contributions of all the lamellae. The axes of the collagen fibrils in successive lamellae typically lie along orthogonal meridians in the medial-lateral and superior-inferior directions²⁴. Therefore, we model the stroma as a summation of layers with half oriented in the medial-lateral direction and half in the superior-inferior direction. For the stroma, we define a coordinate system (x, y, z) with the z -direction orthogonal to the cornea, and the x - and y -directions tangential (medial-lateral and superior-inferior). In the tangential plane $x - y$, the 'isostrain rule' applies similarly to Eq. 9, so by symmetry:

$$C_{xx}^{(\text{stroma})} = C_{yy}^{(\text{stroma})} = \frac{1}{2} C_{11}^{(\text{lamella})} + \frac{1}{2} C_{33}^{(\text{lamella})} \quad (12)$$

The z -direction is orthogonal to the fiber axes in all lamellae, so:

$$C_{zz}^{(\text{stroma})} = C_{22}^{(\text{lamella})} = C_{33}^{(\text{lamella})} \quad (13)$$

In this model, the cornea is transverse isotropic with plane of symmetry $x - y$.

The stress-strain relation of a transverse-isotropic material in the xyz coordinate system can be written as:

$$\begin{bmatrix} \sigma_{xx} \\ \sigma_{yy} \\ \sigma_{zz} \\ \sigma_{yz} \\ \sigma_{yz} \\ \sigma_{xy} \end{bmatrix} = \begin{bmatrix} C_{xx} & C_{xy} & C_{xz} & 0 & 0 & 0 \\ C_{xy} & C_{xx} & C_{xz} & 0 & 0 & 0 \\ C_{xz} & C_{xz} & C_{zz} & 0 & 0 & 0 \\ 0 & 0 & 0 & G_{yz} & 0 & 0 \\ 0 & 0 & 0 & 0 & G_{yz} & 0 \\ 0 & 0 & 0 & 0 & 0 & G_{xy} \end{bmatrix} \begin{bmatrix} s_{xx} \\ s_{yy} \\ s_{zz} \\ s_{yz} \\ s_{xz} \\ s_{xy} \end{bmatrix} \quad (14)$$

Here, G_{yz} ($= G_{xz}$) and G_{xy} correspond to shear moduli in the yz - (xz -) and xy -plane, respectively. By symmetry, $C_{xx} - C_{xy} = 2G_{xy}$, and there are five independent parameters in the stiffness matrix.

Direction-dependent longitudinal modulus

For transverse isotropic materials, there is an analytic expression for the effective longitudinal modulus at an angle θ to the z -axis (assuming material plane of symmetry $x - y$):

$$C(\theta) = \frac{1}{2} [C_{xx} \sin^2(\theta) + C_{zz} \cos^2(\theta) + G_{yz} + D(\theta)] \quad (15)$$

with $D(\theta) = \sqrt{[(C_{xx} - G_{yz}) \sin^2(\theta) - (C_{zz} - G_{yz}) \cos^2(\theta)]^2 + (C_{xz} + G_{yz})^2 \sin^2(2\theta)}$ and mass density ρ . When $\theta = 0$, $C(0) = C_{zz}$, and at $\theta = \pi/2$, $C(\pi/2) = C_{xx}$. This range of possible $C(\theta)$ values characterizes the scale of the anisotropy of the tissue.

We introduce the parameters ε_{xx} , ε_{xz} , and ε_{yz} , defined as:

$$\varepsilon_{xx} = \frac{C_{xx}}{C_{zz}} - 1 \quad (16a)$$

$$\varepsilon_{xz} = \frac{C_{xz}}{C_{zz}} - 1 \quad (16b)$$

$$\varepsilon_{yz} = \frac{G_{yz}}{C_{zz}} \quad (16c)$$

This allows us to rewrite the expression for the longitudinal modulus as follows:

$$C(\theta) = \frac{1}{2} \left[(1 + \varepsilon_{xx}) \sin^2(\theta) + \cos^2(\theta) + \varepsilon_{yz} + \sqrt{[(1 + \varepsilon_{xx} - \varepsilon_{yz}) \sin^2(\theta) - (1 - \varepsilon_{yz}) \cos^2(\theta)]^2 + (1 + \varepsilon_{xz} + \varepsilon_{yz})^2 \sin^2(2\theta)} \right] \quad (17)$$

For soft tissues like the cornea, the shear modulus G_{yz} is typically much smaller than the longitudinal moduli C_{zz} , so $\varepsilon_{yz} \ll 1$. Because the anisotropy of the cornea is also relatively small, $\varepsilon_{xx}, \varepsilon_{xz} \ll 1$. We can expand Eq. 17 to first order in the small parameters $\varepsilon_{xx}, \varepsilon_{xz}$, and ε_{yz} , which yields:

$$C(\theta) \approx C(0)[1 + (2\varepsilon_{xz} + 4\varepsilon_{yz}) \sin^2(\theta) \cos^2(\theta) + \varepsilon_{xx} \sin^4(\theta)] \quad (18)$$

where $C(0) = C_{zz}$ as before.

The anisotropic parameter ε_{xx}

The small parameter ε_{xx} (defined in Eq. 16a) characterizes the degree of anisotropy of a transverse isotropic material. For a single lamella, this anisotropic parameter, $\varepsilon_{11}^{(\text{lamella})}$, is given by:

$$\varepsilon_{11}^{(\text{lamella})} = \frac{C_{11}^{(\text{lamella})}}{C_{33}^{(\text{lamella})}} - 1 \quad (19a)$$

$$= \frac{\left(C_{11}^{(f)} V^{(f)} + C_{11}^{(m)} (1 - V^{(f)})\right) \left(C_{11}^{(m)} V^{(f)} + C_{33}^{(f)} (1 - V^{(f)})\right)}{C_{33}^{(f)} C_{11}^{(m)}} - 1 \quad (19b)$$

If we set $C_{11}^{(m)} = \beta_1 C_{33}^{(f)}$ and $C_{11}^{(f)} = \beta_2 C_{33}^{(f)}$, we obtain:

$$\varepsilon_{11}^{(\text{lamella})} = \frac{\left(\beta_2 V^{(f)} + \beta_1 (1 - V^{(f)})\right) \left(\beta_1 V^{(f)} + 1 - V^{(f)}\right)}{\beta_1} - 1 \quad (20)$$

The anisotropic parameter ε_{xx} for a stack of orthogonal lamella is given by:

$$\varepsilon_{xx}^{(\text{stroma})} = \frac{C_{xx}^{(\text{stroma})}}{C_{zz}^{(\text{stroma})}} - 1 = \frac{C_{11}^{(\text{lamella})} + C_{33}^{(\text{lamella})}}{2C_{33}^{(\text{lamella})}} - 1 \quad (21a)$$

$$= \frac{\varepsilon_{11}^{(\text{lamella})}}{2} \quad (21b)$$